

See discussions, stats, and author profiles for this publication at: <https://www.researchgate.net/publication/231230267>

# Dynamics of Methane–Propane Clathrate Hydrate Crystal Growth from Liquid Water with or without the Presence of n-Heptane

ARTICLE in CRYSTAL GROWTH & DESIGN · APRIL 2006

Impact Factor: 4.89 · DOI: 10.1021/cg0600647

CITATIONS

30

READS

31

4 AUTHORS, INCLUDING:



**Ju Dong Lee**

Korea Institute of Industrial Technology

51 PUBLICATIONS 966 CITATIONS

SEE PROFILE



**Myungho Song**

Dongguk University

8 PUBLICATIONS 119 CITATIONS

SEE PROFILE



**Peter Englezos**

University of British Columbia - Vancouver

182 PUBLICATIONS 4,844 CITATIONS

SEE PROFILE

# Dynamics of Methane–Propane Clathrate Hydrate Crystal Growth from Liquid Water with or without the Presence of *n*-Heptane

Ju Dong Lee,<sup>†</sup> Myungho Song,<sup>‡</sup> Robin Susilo,<sup>†</sup> and Peter Englezos<sup>\*,†</sup>

*Department of Chemical and Biological Engineering, University of British Columbia,  
2360 East Mall, Vancouver, British Columbia, V6T 1Z3, Canada, and*

*Department of Mechanical Engineering, Dongguk University, Chung-gu, Seoul, 100-715, Korea*

*Received February 7, 2006; Revised Manuscript Received March 15, 2006*

**ABSTRACT:** Methane–propane clathrate hydrate crystal growth within an enclosure partially filled with liquid water was examined under different undercooling conditions both with and without the presence of *n*-heptane. Water saturated with guest gas was rapidly undercooled and maintained at constant temperature. The growth of the hydrate phase always started with the formation of a film at the upper surface of the liquid water pool. The visual observations using a microscope revealed detailed features of crystal nucleation, migration, and growth occurring within the water pool. In all experiments, hydrate crystal growth was initiated by the formation of hydrate film at the interface between liquid water and the adjacent gas or *n*-heptane layer. Hydrate crystals were then observed to grow downward from the film. Undercooling was found to be a key parameter to control the morphology of hydrates growing underneath the hydrate film as it influences the growth rate and configurations of crystals. Moreover, a number of small crystals were seen in the water ascending toward the hydrate film. The evolution of the shape of these crystals was monitored. These crystals were octahedral or triangular or hexagonal platelets. Finally, the role of constitutional undercooling and the memory of the water to the observed crystal growth are discussed.

## Introduction

Gas hydrates (or more precisely clathrate hydrates) are nonstoichiometric solid compounds, which consist of a framework structure of water molecules and inclusion molecules such as natural gas components. The water molecules are called the host molecules and are linked to each other through hydrogen bonding to form polyhedral cavities. The molecules that fill the cavities are called the guest molecules, which have to be small enough to fit into the cavity. As the presence of guest molecules stabilizes the framework structure, gas hydrates form at a relatively higher temperature than the freezing temperature of pure water if sufficiently high pressure is imposed.<sup>1–3</sup> Hydrates crystallize in two structures known as I and II.<sup>3</sup> Another structure that requires the presence of a large molecule guest substance (LMGS) to form was discovered at National Research Council (NRC) of Canada.<sup>4,5</sup>

Gas hydrate formation in general is a complex multiphase crystallization process. The identification of the relevant phases as well as their measurement and analysis requires microscopic (X-ray diffraction, NMR, etc.) and macroscopic techniques such as thermodynamics, gas uptake measurements, and morphology.<sup>1,3,6–8</sup> Morphology is concerned with the shapes and sizes of forming and decomposing hydrate phase boundaries, whose length scales are much larger than molecular structure and much smaller than system dimensions. The knowledge of micro-level study obtained from various diffraction crystallography and spectroscopy analyses provides the changes or transition of the structure, composition and cage occupancy, and molecular orientation. Together with the experimental results of phase equilibrium measurements, thermophysical properties such as density, hydration number, and enthalpy of phase change are determined under the assumption that molecular structure is uniform and free of defects. However, hydrate is seldom uniform

unless it is formed from a single seed crystal at an extremely slow growth rate. Because of atomic scale defects such as dislocations and vacancies, which strongly interact with grain boundaries created by multiple nucleation and unstable advances of growth front, macroscopic characteristics of bulk hydrates may be quite different from those of a single hydrate crystal. The information provided by morphology studies has been useful in estimating the macroscopic flow characteristics such as permeability of bulk crystals and transport characteristics such as effective thermal and solute diffusion coefficients in bulk crystals in metallurgical systems either fully solidified or undergoing phase changes.<sup>9</sup>

Morphological observations have also contributed toward the mechanistic understanding of hydrate crystal growth. For example, Ohmura et al.<sup>10</sup> correlated the observed morphology of CO<sub>2</sub> hydrate with a nondimensional index assuming mass transfer control of crystal growth. Lee et al.<sup>11</sup> studied water droplets immersed in methane–ethane and methane–propane gas mixtures and observed a lateral growth stage lasting about 10–23 s followed by a slow growth stage at the hydrate–water and hydrate–gas interfaces. Makogon et al.<sup>12</sup> studied tetrahydrofuran (THF) hydrate as an analogue of structure II natural gas hydrates and their kinetic inhibition. Larsen et al.<sup>13</sup> reported results for ethylene oxide hydrate as an analogue of methane hydrate (structure I). Smelik and King investigated the crystal growth behavior of structure I, II, and H using a specially designed optical cell and observed that each structure type exhibits characteristic crystal morphology.<sup>14</sup> Majority of morphology studies concerned single gas hydrates and hydrate formation from gas–liquid systems. Servio and Englezos<sup>15</sup> and Ohmura et al.<sup>16</sup> studied structure H hydrate formation that involves a third fluid (liquid) phase.

In this work, we present a new experimental apparatus that offers the ability to monitor crystal growth at bulk interfaces with a significant level of detail. The system involves methane–propane hydrate with or without the presence of *n*-heptane. A gas mixture of 90.5% methane balanced with propane is used

\* Corresponding author. Tel: 1-604-822-6184. Fax: 1-604-822-6003.

<sup>†</sup> University of British Columbia.

<sup>‡</sup> Dongguk University.

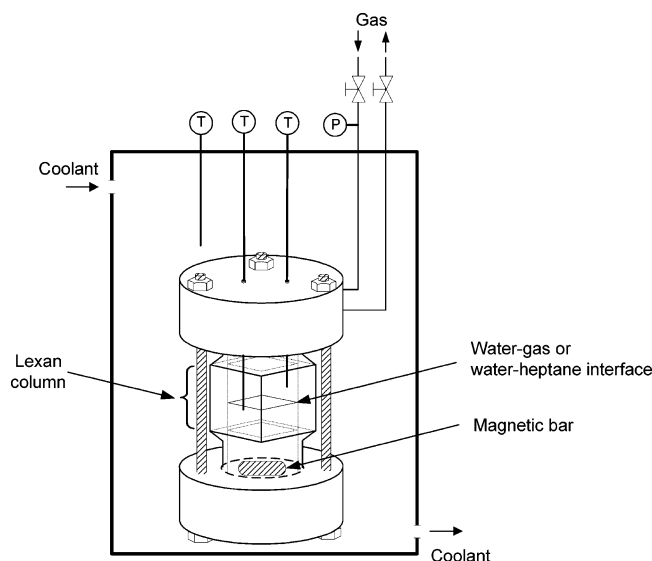


Figure 1. Morphology apparatus.

as the guest molecule, which is known to form structure II hydrate.<sup>17–21</sup> These hydrocarbon gas mixtures are relevant to the design of facilities for storage and transport of natural gas in the form of hydrates, as known as gas to solids technology (GTS).<sup>22,23</sup> During the experiment, the nucleation, crystal growth, and migration of gas hydrate have been extensively examined through observation at a stationary interface between water and gas as well as water and *n*-heptane at different degrees of undercooling.

### Experimental Apparatus and Procedures

The schematic of the apparatus utilized for the present study is shown in Figure 1. The high pressure test assembly is a hollow polycarbonate (Lexan) column closed at the top and bottom ends by stainless steel (SS) lids. The entire test assembly is immersed in a temperature-controlled water bath which was made of 10-mm-thick Plexiglas to allow for the visual access from the outside.

The Lexan column has upper, middle, and lower portions that have the same vertical length of 25 mm but different horizontal cross-sections. In a plane view, the outer surface of the middle portion is a 37-mm square, and the inner cavity is a 25-mm square with rounded corners. Therefore, the middle portion consists of four identical vertical windows. Since the approximately 15-mm-wide center sections of these windows were flat and of uniform thickness, undistorted images of crystal nucleation, migration, growth, and decomposition could be obtained through the hand polished inner and outer surfaces. The lower portion of the column is a hollow cylinder having an outer diameter of 37 mm and an inner diameter of 25 mm. The outer surface of the upper portion is the same as that of the lower portion and the inner cavity of the upper portion is the same as that of the middle portion.

The top and bottom lids were stainless steel cylindrical plates having the dimensions of 44 mm in height and 114 mm in outer diameter. Both lids have carved space into which the upper and lower portions of the Lexan column fit snugly. Between the Lexan column and each lid, one pair of O-rings were placed to seal the test cavity. Top lid has sealed ports for gas feeding and releasing lines, for illuminating borescope and for copper-constantan thermocouples to measure the temperature of liquid and gas phases inside the test cell. An additional thermocouple was employed to monitor the bath temperature. The gas feeding line was connected to a digital pressure indicator. A magnetic bar for the agitation of the liquid phase was placed at the bottom of the test cell. A halogen light source with gooseneck was installed outside the water bath and served as an alternative source of light. A microscope (Nikon, SMZ1000) attached either with a CCD video camera (Sony, DXC-390) or digital camera (Nikon, Coolpix 5400) was used to record the picture or video images during the experiment run.

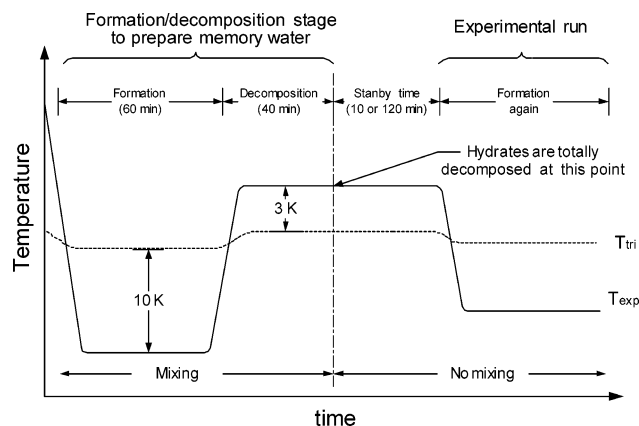


Figure 2. Temperature-time diagram illustrating the two stages during an experiment.

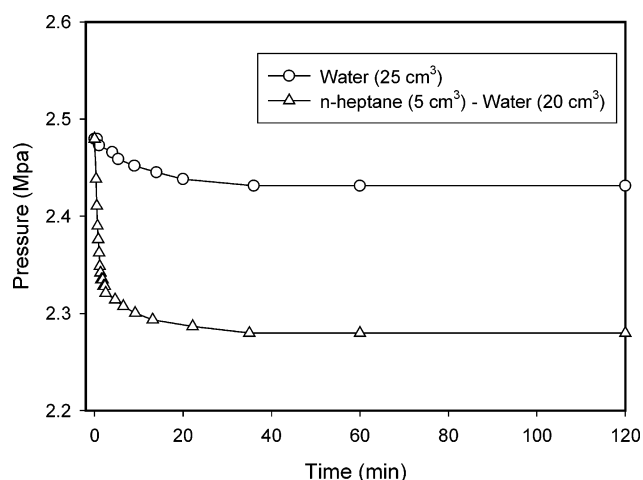


Figure 3. Preliminary experiment for the saturation of the liquid phase (water or heptane-water) with guest substance (methane-propane gas) at 2.48 MPa and 286.7 K.

Each experimental run was commenced by injecting 25 cm<sup>3</sup> of liquid water into the test cell. In the case of the water and *n*-heptane system, 20 cm<sup>3</sup> of water and 5 cm<sup>3</sup> of *n*-heptane were used. The test cell is then flushed at least three times with the hydrate forming gas to remove any residual air. The experimental procedure is divided into two stages as shown in Figure 2. A hydrate formation/decomposition stage is carried out to prepare memory water. Memory water is a term that refers to water that has been used to form hydrates. It is known to reduce the induction time in subsequent experiments. Hydrates are then formed again with memory water in the second stage. The experimental temperature ( $T_{\text{exp}}$ ) and hydrate equilibrium temperature ( $T_{\text{tri}}$ ) along with time are also presented in Figure 2.

Prior to each experimental run, the hydrate forming gas was fed until it reached the desired pressure above the hydrate equilibrium condition, and then the medium was rapidly undercooled and maintained at the constant temperature, typically 10 K below the  $T_{\text{tri}}$ . Along with the undercooling, the liquid in the test cell was fully saturated with guest gas molecules by mixing with the help of a rotating magnetic bar. As shown in Figure 3, 30 min of mixing is sufficient to saturate the liquid with guest species regardless of the presence of *n*-heptane. After the system temperature was dropped below  $T_{\text{tri}}$ , hydrate formation was initiated and the hydrate crystals were allowed to grow for 1 h at constant temperature and pressure. Subsequently, the hydrate crystals grown in the test cell were dissociated by increasing the temperature approximately 3 K above  $T_{\text{tri}}$ . Typically 40 min were required for the complete dissociation of hydrate crystals. It is noted that all experiments were done without adding or releasing any gas, and agitation was employed continuously during the decomposition period. After no hydrate particles could be seen from the liquid solution, the liquid was

**Table 1.** Experimental Conditions and the Time Required for the First Appearance of Downward Hydrate Crystals. The Liquid Pool in Experiments 1 to 4 was Water and in Experiments 5 to 8 was Water + Heptane<sup>a</sup>

exp	liquid pool	$P_{\text{exp}}$ (MPa)	$T_{\text{exp}}$ (K)	$T_{\text{tri}}$ (K)	final C1 comp <sup>b</sup> (%)	$\Delta T$ ( $T_{\text{tri}} - T_{\text{exp}}$ ) (K)	$T_{\text{down}}^c$ (min)
1	water only	3.72	274.5	289.7	90.8	15.2	1
2		3.22	274.9	288.6	90.7	13.7	3
3		2.40	278.2	286.3	90.5	8.1	15
4		1.43	278.7	281.9	90.6	3.2	N/A
5	water + heptane	3.72	274.5	289.0	92.7	14.5	3
6		3.22	274.9	287.9	92.5	13.0	5
7		2.40	278.2	285.4	92.7	7.2	90
8		1.43	278.7	281.1	92.6	2.4	N/A

<sup>a</sup> Each experiment was carried out with memory water, which aged for two hours at 3 K above hydrate equilibrium temperature. Initial hydrate forming gas was a mixture of 90.5% methane (C1) and 9.5% propane (C3).

<sup>b</sup> Gas-phase composition was measured after experimental run. <sup>c</sup> Time required for the first appearance of downward hydrate crystal after hydrate film formation.

kept for 2 h without any mixing. We refer to this period as standby time. In some experiments as listed in Table 2, the liquid was kept for

**Table 2.** Supplementary Experiments for Floating Hydrate Crystals<sup>a</sup>

exp	liquid pool	$P_{\text{exp}}$ (MPa)	$T_{\text{exp}}$ (K)	$T_{\text{tri}}$ (K)	final C1 composition (%)	$\Delta T$ ( $T_{\text{tri}} - T_{\text{exp}}$ ) (K)
9	water only	3.22	274.9	288.6	90.7	13.7
10		2.40	278.2	286.3	90.5	8.1
11	water + heptane	3.72	274.5	289.0	92.7	14.5

<sup>a</sup> Each experiment was carried out with memory water. The standby time was 10 min at 3 K above hydrate equilibrium temperature. Initial hydrate forming gas was a mixture of 90.5% methane (C1) and 9.5% propane (C3).

10 min to study the effect of history in memory water (i.e., standby time is 10 min).

The water solution that has experienced hydrate formation was then used for all subsequent morphological experiments. In the second stage as described in Figure 2, the system temperature was cooled to a desired point to induce hydrate reformation. Subsequently, the formation and growth of hydrate crystals were monitored and recorded by a microscope connected with video camera.

In this study, the hydrate forming gas was a mixture of 90.5% methane (C1) and 9.5% propane (C3). The composition was analyzed by gas chromatography (Varian, CP-3800). The hydrate equilibrium

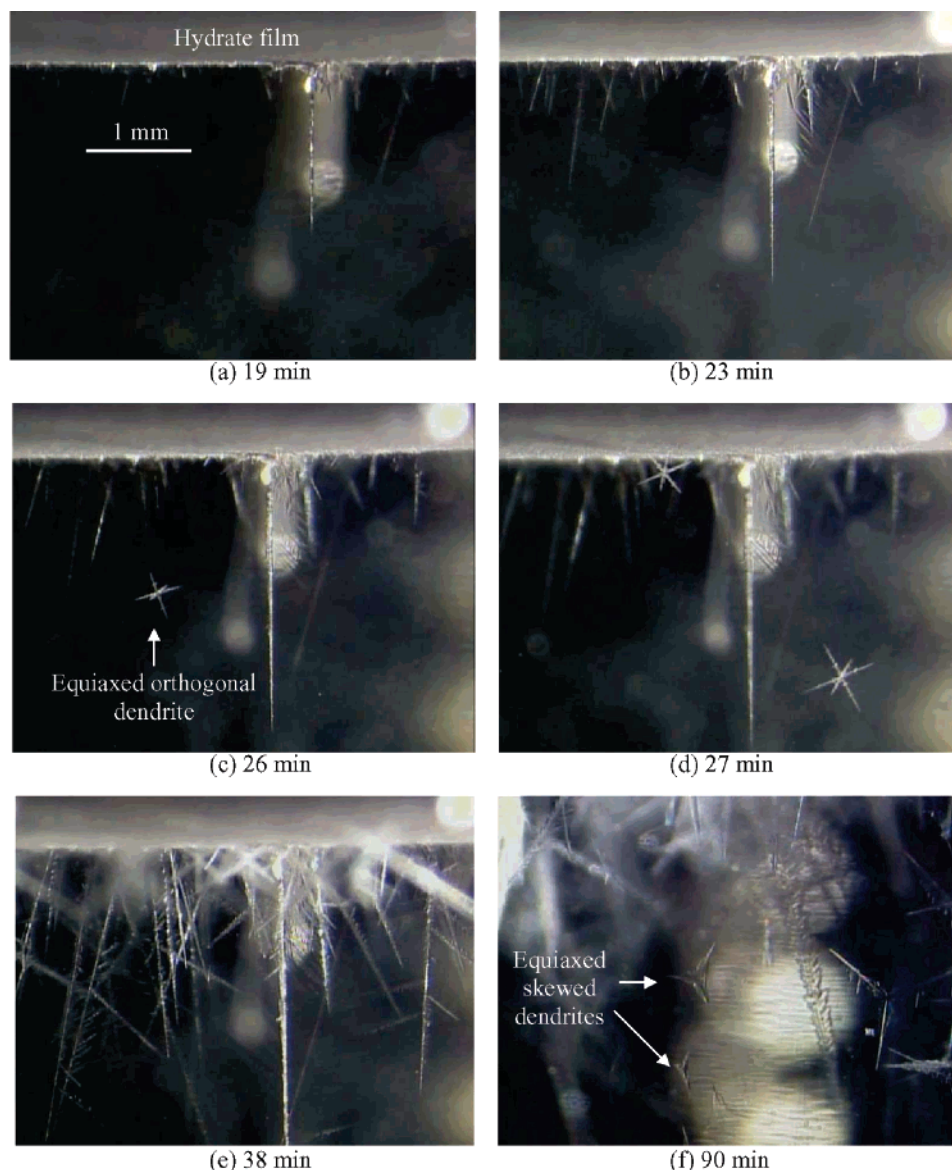


**Figure 4.** Sequential images of the crystals during hydrate formation from the methane–propane–water system at 3.22 MPa,  $T = 274.9$  and 13.7 K undercooling (experiment 2). The time lapse after the formation of hydrate film is indicated below each image. The microscope focused 1 cm below the interface in (f).



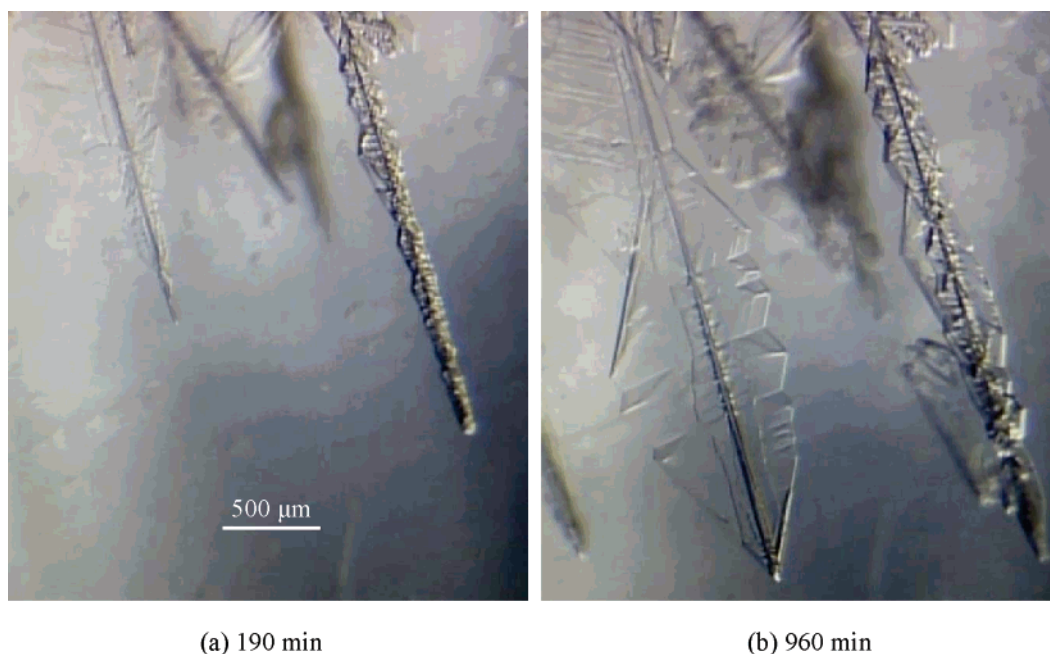


**Figure 5.** Development of the tip of the downward crystal (experiment 2). The time lapse after the formation of the hydrate film is indicated below each image.

temperature ( $T_{\text{tr}}$  in Tables 1 and 2) corresponding to the system pressure and final gas-phase composition was calculated by using the CSMHYD program.<sup>2</sup>

### Results and Discussion

Morphological observations of methane–propane (C1C3) hydrates were made under different undercooling,  $\Delta T$  (magnitude of driving force in terms of the difference between equilibrium and experimental temperatures) with and without the presence of *n*-heptane (nC7). The experimental conditions and the time required for the first appearance of downward hydrate crystals after hydrate film formation are summarized in Table 1. The change of gas composition was also presented. It was noticed that propane dissolves more in the liquid phase, especially in the presence of *n*-heptane.

In all experiments, hydrate crystal growth was initiated by the formation of hydrate film at the interface between liquid water and the adjacent gas or *n*-heptane layer. The induction time for crystallization was found to vary between 30 and 120 min. Once nucleation starts, the interface is covered with crystal within 30 s. Hydrate crystals were then observed to grow downward from the film. Undercooling is found to be a key parameter to control the morphology of hydrates growing underneath the hydrate film as it influences the growth rate and configurations of crystals.

**The Methane–Propane–Water System.** Figure 4 shows a typical sequence of hydrate growth observed at the gas–water interface during experiment 2. The spicular hydrate crystals were seen growing downward from the hydrate film, and then they grew into a dendritic shape. As crystal growth progressed, the speed of the downward crystal growth retarded, and thin flanges grew from the tips and sides of the first-grown hydrate crystals, which are shown in Figure 5. The morphology of hydrate crystals during experiments 1 and 3 showed similar growth patterns as in experiment 2, but as the  $\Delta T$  increased, the growth rate and arm spacing of the downward crystals became greater and finer. The observed configurations of the methane–propane

hydrate crystals growing from the hydrate film conform with reported morphology of CO<sub>2</sub>–water or methane–water systems.<sup>10,24</sup>

An interesting observation was made during the present study. In particular, crystals were seen floating from the bottom of the enclosure to the hydrate film at the interface and interacted with downward growing hydrate crystals which originated from the hydrate film. The typical floating crystals observed during experiment 2 have two distinct shapes, equiaxed orthogonal dendrite (EOD) and equiaxed skewed dendrite (ESD). During the early stage of experiment, only EOD crystals ascended from the bottom, and then ESD floating crystals also appeared as shown in Figure 4c,d,f. Further discussion regarding the floating crystals is presented in the next section.

Figure 6 shows the observations of hydrate crystal growth made during experiment 4 at the lowest undercooling ( $\Delta T = 3.2$  K). Hydrate film was also seen to appear first at the interface. However, no significant downward crystal growth was observed after the formation of hydrate film. Under minimum undercooling conditions employed, floating crystals from the bottom of the test cell were small polyhedral particles. The crystals were seen constantly floating up to 350 min after film formation. The shape and size of floating crystals were examined with high magnification. Most of the floating crystals had octahedral shape (eight triangular faces), arranged like two pyramids connected at their bases. These octahedra were rather uniform in size (30–40  $\mu\text{m}$ ) and had approximately 0.7 mm/min of upward speed. As seen in Figure 6, they settled at the hydrate film where some of them slowly grew and assumed a columnar shape. The growth rate was much smaller than that observed in experiment 2.

**The Methane–Propane–Heptane–Water System.** The influence of *n*-heptane on methane–propane hydrate formation was investigated through experiments 5–8. Since *n*-heptane is immiscible and lighter than water, the discrete *n*-heptane layer forms above the liquid water pool. *N*-Heptane is known not to serve as guest species but mainly interferes with mass transport between gas phase and liquid water pool.

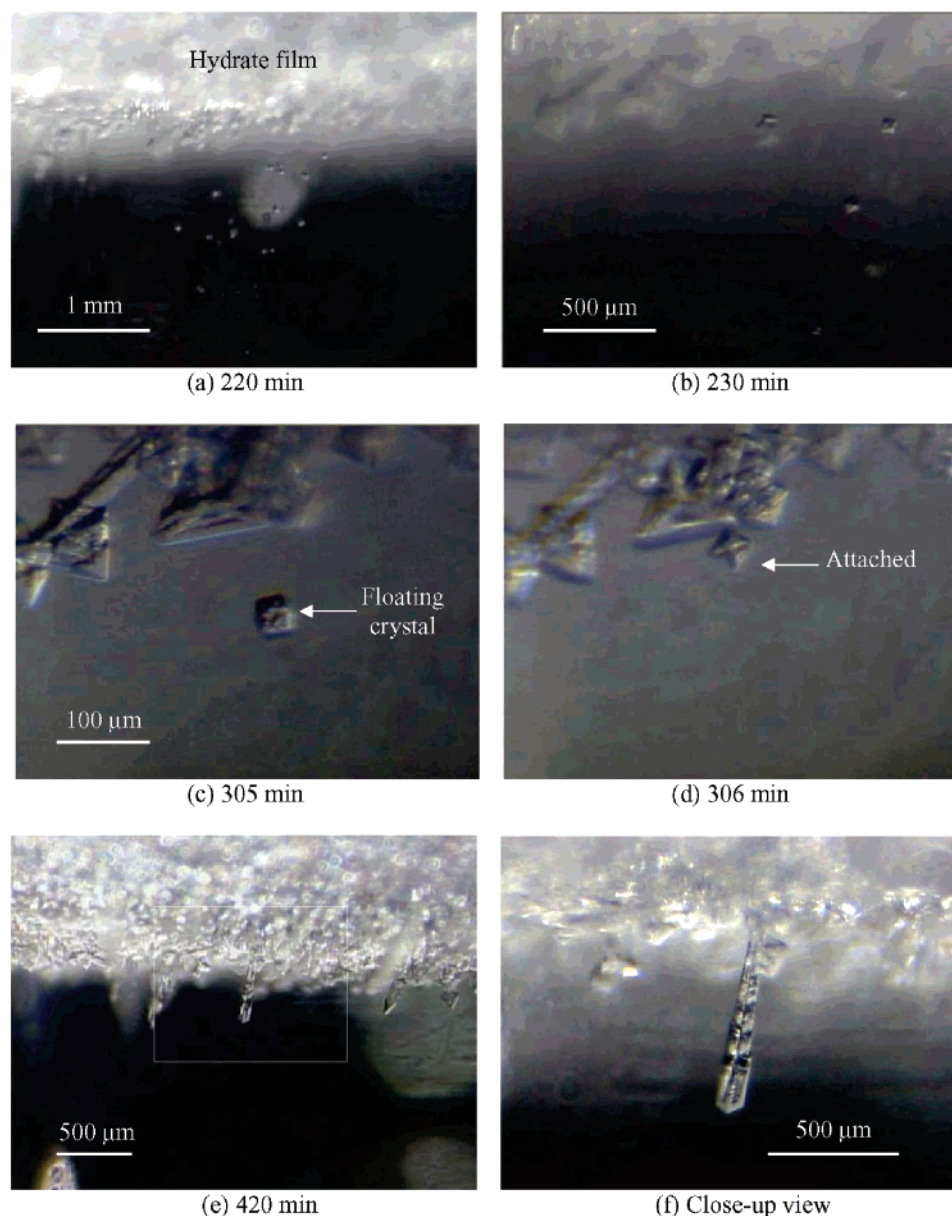


**Figure 6.** Sequential images of the crystals during hydrate formation from the methane–propane–water system at 1.43 MPa, 278.7 and 3.2 K undercooling (experiment 4). The time lapse after the formation of hydrate film is indicated below each image. Image (f) is magnified from (e).

The hydrate film also appeared at the interface between the liquid water and *n*-heptane. The sequential images for the subsequent downward crystal growth at 14.5 and 7.2 K undercooling are shown in Figures 7 and 8, respectively. They were qualitatively the same as those of the system without *n*-heptane. Figure 8 indicates that thin flanges developed from the tips and sides of the downward growing crystals during experiment 7. The crystals have a growth pattern similar to those shown in Figure 5. When the lowest driving force (experiment 8) was applied, the observations were comparable to those from the C1C3–water system (experiment 4), where the downward growth was not noticed and the polyhedral type floating crystals were also observed. The qualitative behavior of floating crystals was not affected by the presence of *n*-heptane.

To examine the influence of *n*-heptane quantitatively, the lengths of the hydrate crystals were determined from the captured video images. The results shown in Figure 9 clearly indicate that axial growth rates are almost constant at the early

stage of an individual experiment run and strongly depend on  $\Delta T$ . The hydrate growth rate in the presence of *n*-heptane was relatively smaller compared to the value without heptane possibly due to the additional mass transfer resistance offered by heptane layer.

**Observation of Floating Hydrate Crystals.** As mentioned in the previous section, floating hydrate crystals were seen in every hydrate forming experiment discussed here. Their shapes and sizes are mainly determined by the degree of undercooling and time. During duplicate experiments to elucidate the behavior of the floating crystals, it was found that the number of floating crystals was strongly related with the memory of water. Experiments with a short standby time induced more floating hydrates compared to those with longer periods. The conditions for those experiments with a short standby time are listed in Table 2, and the visual observations are presented in Figures 10–12. Each experiment was conducted using hydrate-dissociated



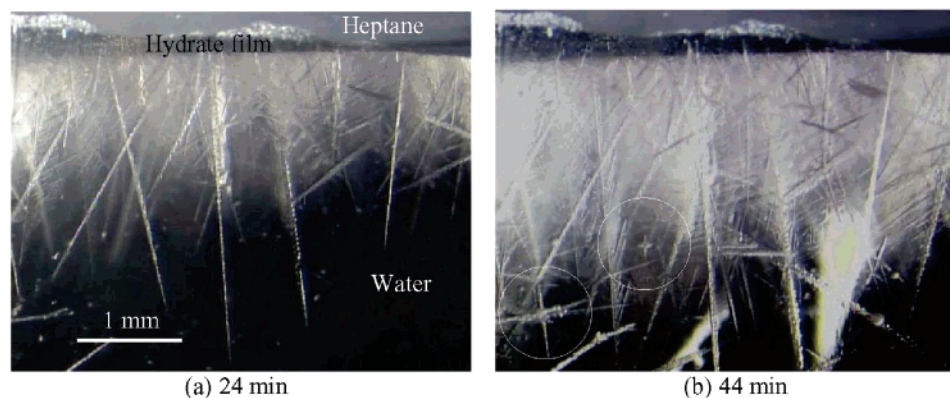


**Figure 7.** Sequential images of the crystals during hydrate formation from the methane–propane–heptane–water system at 3.72 MPa, 274.5 and 14.5 K undercooling (experiment 5). The time lapse after the formation of the hydrate film is indicated below each image. Floating crystals are indicated by circles in (b).

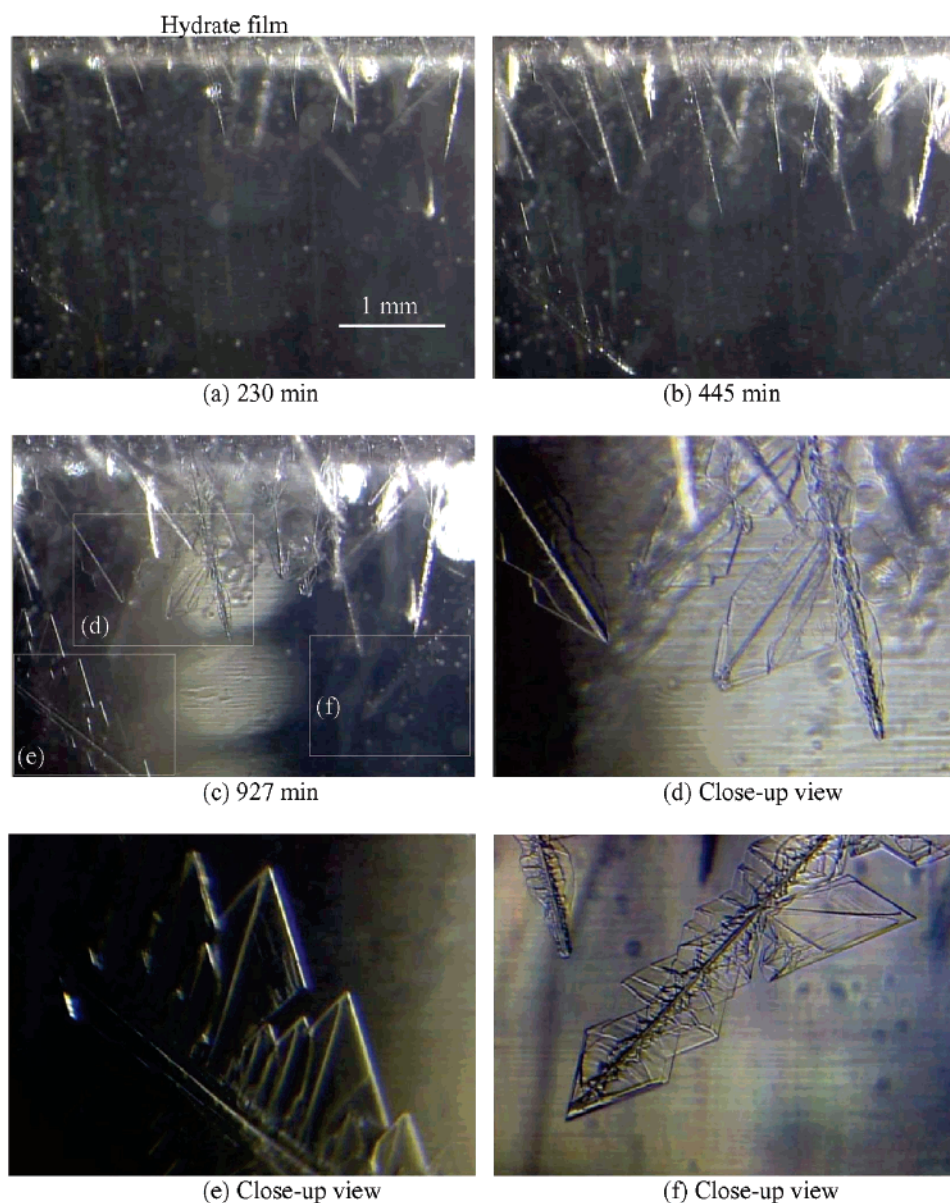


**Figure 8.** Sequential images of the crystals during hydrate formation from the methane–propane–heptane–water system at 2.40 MPa, 278.2 and 7.2 K undercooling (experiment 7). The time lapse after the formation of the hydrate film is indicated below each image. Images (d–f) are magnified (c) 2.5 times.

water (memory water) which remained in the dissociated state for 10 min (standby time). It is noted that floating crystals

were observed after the appearance of the hydrate film at the interface.

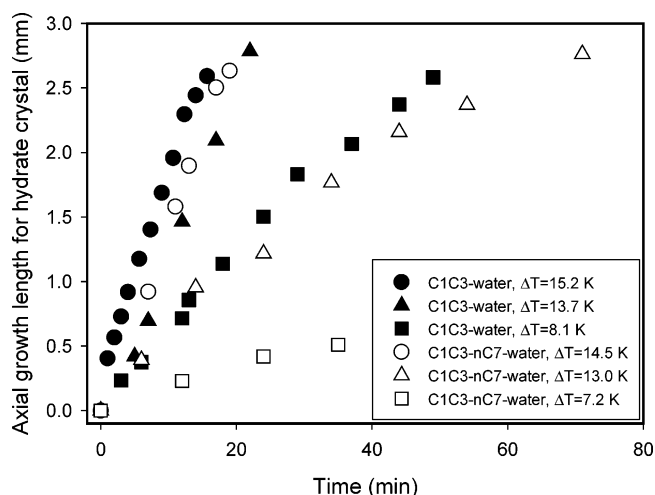


**Figure 9.** Axial growth length for the downward hydrate crystals. The hydrate formation conditions are presented in Table 1.

Figure 10 shows equiaxed orthogonal dendrites (EOD) ascending from the bottom and settled underneath the hydrate film. EOD have six almost identical and mutually orthogonal primary arms. While floating from the bottom, primary arms lengthened and secondary arms developed from the primary arm at right angles. Occasionally, two or more EOD were found to have grown together; thus more complex shapes are possible. Larger crystals ascended faster than the smaller ones with the ascending speed ranging from 1 to 4 mm/min corresponding to the crystal size ranging approximately between 0.2 and 1.2 mm. At later times, the floating crystals having different orientation might pile up below the hydrate film and interact with each other as shown in Figure 10e,f.

When one of the EOD crystals reached the hydrate film, the primary arm closest to the downward direction grew faster than the other primary arms as shown in Figure 11a,b. Simultaneously, secondary arms were developed from the extended primary arm, and they became thicker and longer as crystallization progressed (Figure 11c,d). Afterward, different types

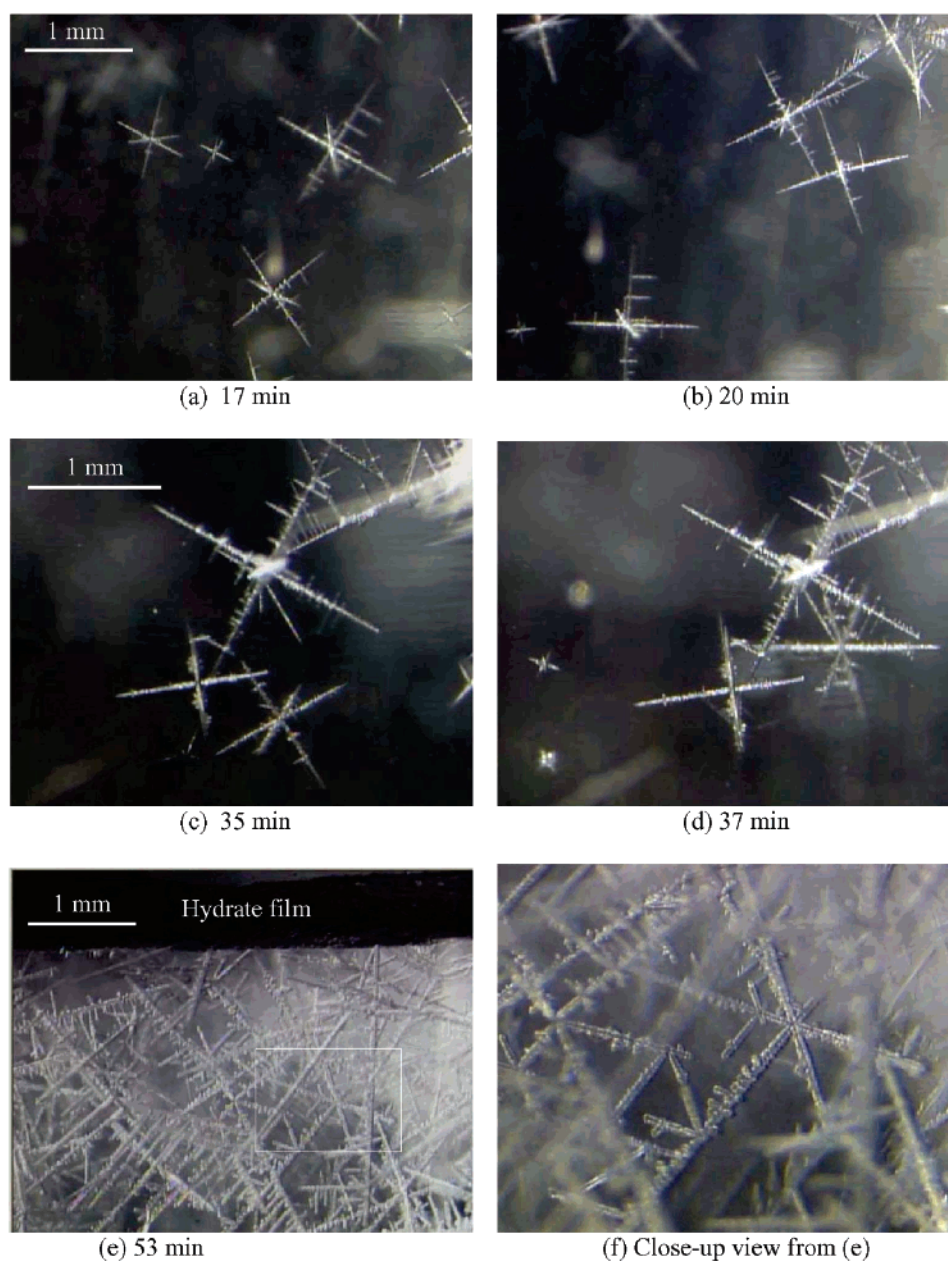


**Figure 10.** Sequential images of floating crystals during hydrate formation from the methane–propane–water system at 3.22 MPa, 274.9 and 13.7 K undercooling (experiment 9). The time lapse after the formation of hydrate film is indicated below each image.



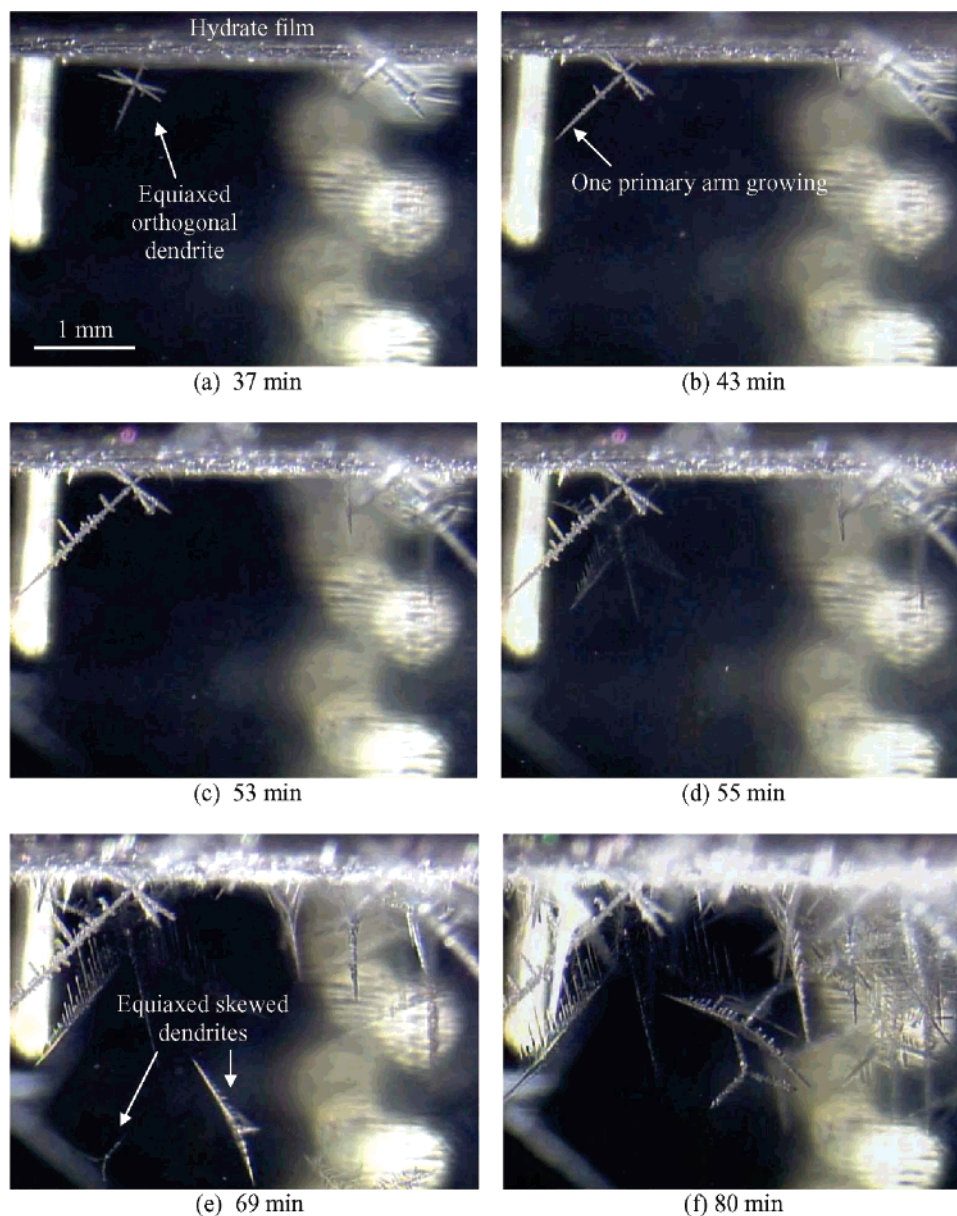


**Figure 11.** Sequential images of floating crystals during hydrate formation from the methane–propane–water system at 2.40 MPa, 278.2 and 8.1 K undercooling (experiment 10). The time lapse after the formation of hydrate film is indicated below each image.

of crystals also arrived from the bottom and grew together (Figures 11e,f and 12). These are called equiaxed skewed dendrite (ESD) crystals. They have three primary arms developing on the same coordinate plane.

It is obvious from our observations that hydrate crystals are able to grow during migration in the bulk phase as well as stagnant near the hydrate film. When the floating hydrate crystals reached the hydrate film, the equiaxed growth is no longer sustained because the preferred growing direction becomes downward. If downward hydrate growth from the hydrate film is not active, the settled floating crystals further reduce the chance for the downward crystal growth as the guest species near hydrate film is exhausted by the growth of migrated crystals. Otherwise, the growth of hydrate crystal underneath the hydrate film becomes more complex with crystals having different origins compete with each other. The typical examples of the former case are shown in Figure 11a–d, while the latter case examples are shown in Figure 11e and primarily 11f.

**Origin of Floating Crystals.** To establish what the origin of floating crystals is and how they grow in the bulk water phase,

duplicate experiments were performed in which individual floating crystals in the bulk phase were carefully observed. In the early stage of hydrate formation, a few small octahedral crystals and two-dimensional triangular or hexagonal platelets were observed especially in the lower part of the liquid water pool. The number of floating crystals decreased in the following order: octahedra > triangular platelets > hexagonal platelets. Figure 13 shows the development of floating crystals in the liquid water pool at 13.7 K undercooling. It is clear that the primary arms of EOD crystals developed from each vertex of the octahedron, and those of ESD developed from the vertexes of a platelet. The secondary arms were developed from primary arms. It is noteworthy that the secondary arms of EOD develop at right angles with primary arm, but the secondary arms of ESD are skewed and parallel with the adjacent primary arm.

So far, all experiments were done using memory water. Thus, one additional issue to be addressed is whether the floating crystals will occur in the case of freshwater (water without hydrate memory). An additional experiment was performed with freshwater. In this case, a wire mesh (sieve size no. 60) was

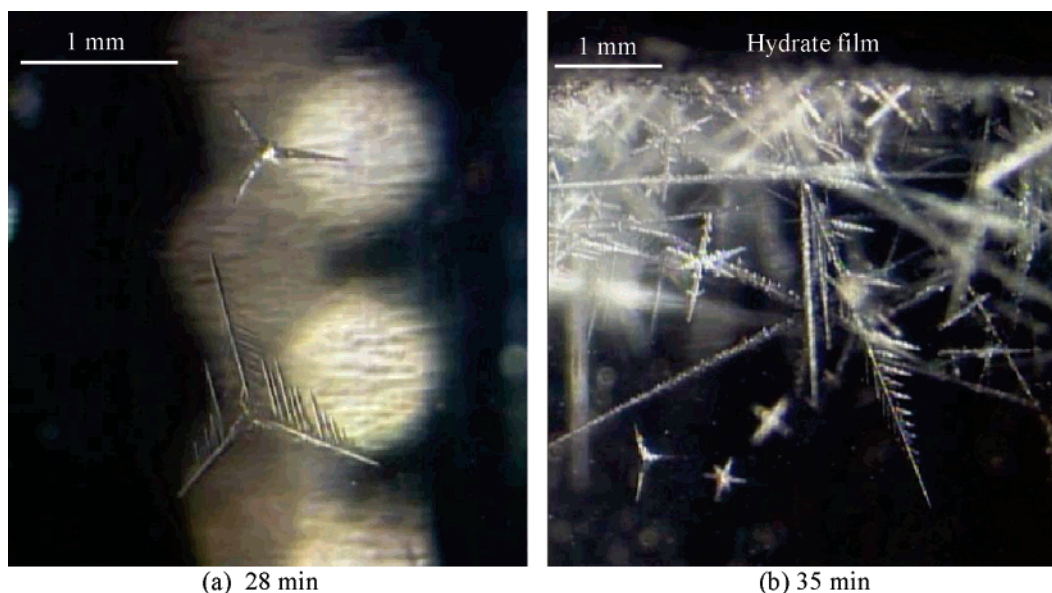


**Figure 12.** Sequential images of the floating crystals during hydrate formation from the methane–propane–heptane–water system at 3.72 MPa, 274.5 and 14.5 K undercooling (experiment 11). The time lapse after the formation of the hydrate film is indicated below each image.

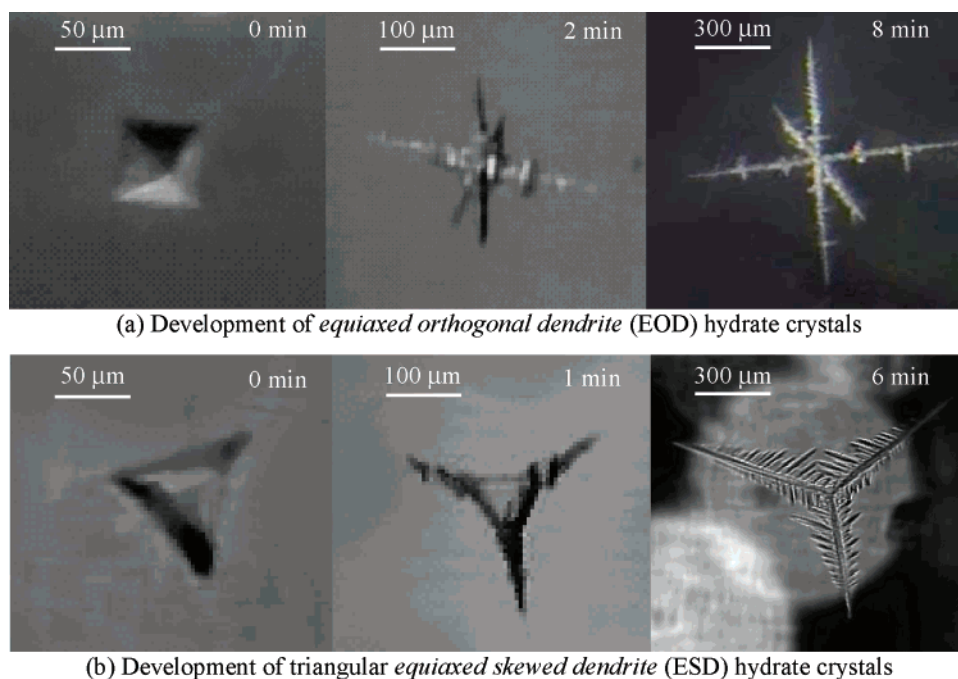


**Figure 13.** Development of floating crystals in liquid water pool. Hydrate crystals grown at 3.22 MPa, 274.9 and 13.7 K undercooling from the methane–propane–water system. (a) Octahedron → primary arms → secondary arms developed as crystallization progressed. (b) Triangular thin platelet → primary arms → secondary arms developed as crystallization progressed.

used to trap the floating crystals. The experiment followed the same procedure as described in the experimental section, but the procedure to produce memory water was omitted. After saturation with guest molecules, the water was undercooled, and subsequently observations were made. Some floating crystals ascended through the mesh, but a majority of crystals were trapped as seen in Figure 14. The important outcomes from this additional experiment are as follows. First, the floating crystals can nucleate regardless of memory. Second, the number of floating crystals is significantly large when memory water is utilized. Finally, the floating crystals mainly originate from the lower half of the enclosure.

**Growth Rate of Primary Arm.** The growth rates of the primary arm were determined based on visual observations in

some experiments, and the results are shown in Table 3. On the basis of these limited and difficult to obtain data, it is seen that the growth in ESD is the fastest. As seen from the pictures, six primary arms were developed from octahedra and three primary arms branched from the triangular platelets. Because of these compact occurrences of primary arms, the amount of guest species (methane and propane) available near the octahedron is less than near the platelets. Consequently, the growth rate of EOD primary arm is slower than that of ESD. The rare availability of guest species is also probably responsible for the slower growth rate in the case of downward crystals. This study was done under quiescent conditions, and thus mass and heat transfer are expected to be restrained. One is then not able to distinguish between intrinsic kinetic and transport phenomena



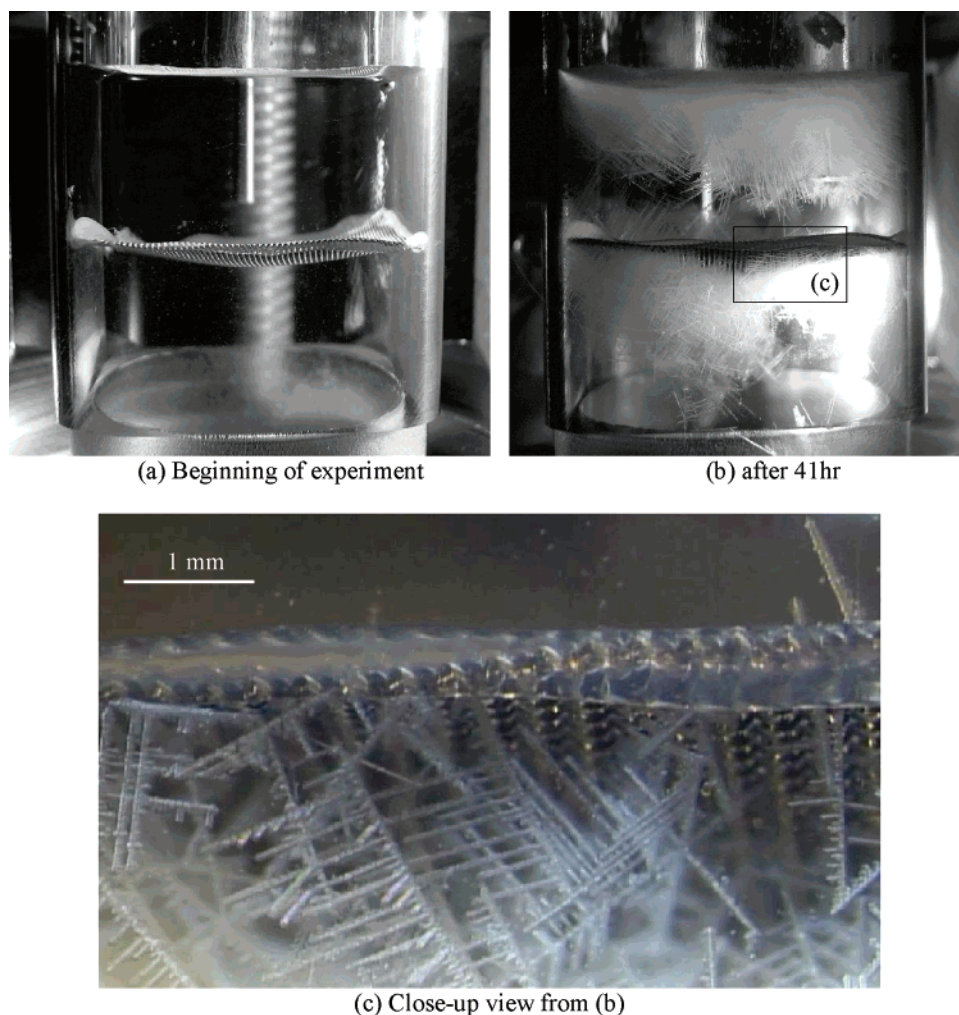


**Figure 14.** Hydrate formation from freshwater at 3.72 MPa, 274.5 and 13.7 K undercooling with a stainless steel screen.

**Table 3.** Comparison of Growth Rates of the Primary Arm for Different Crystal Types Found in This Study<sup>a</sup>

exp no.	crystal type	growth rate of primary arm ( $\mu\text{m}/\text{min}$ )
2	downward crystal	58
9	equiaxed orthogonal dendrite (EOD)	89
9	equiaxed skewed dendrite (ESD)	102

<sup>a</sup> $P = 3.22 \text{ MPa}$ ,  $T = 274.9 \text{ K}$ ,  $\Delta T = 13.7 \text{ K}$ . The growth rate was measured during the 10 min following the first development of primary arms

effects. Hydrates from light natural gas constituents are believed to exhibit intrinsic kinetic effects.<sup>25–27</sup> If heat and mass transfer become drastic, e.g., by vigorous agitation, both thermal and solute gradient in front of the hydrate/liquid interface diminish. Since then constitutional undercooling cannot be sustained, intrinsic kinetics dominates the crystal growth. Constitutional undercooling is discussed in the next section.

**Discussion for Nucleation and Growth Morphology.** In this subsection, theories widely accepted in metallography are applied to the formation of gas hydrate to gain the insight of experimental observations made during the present study. Our discussion is confined to the hydrate growth from liquid water only. It should be pointed that the morphology of hydrate formed from ice or vapor water also requires attention because these options may be favored for the mass production of hydrate. For example, the most common technique to prepare the specimen

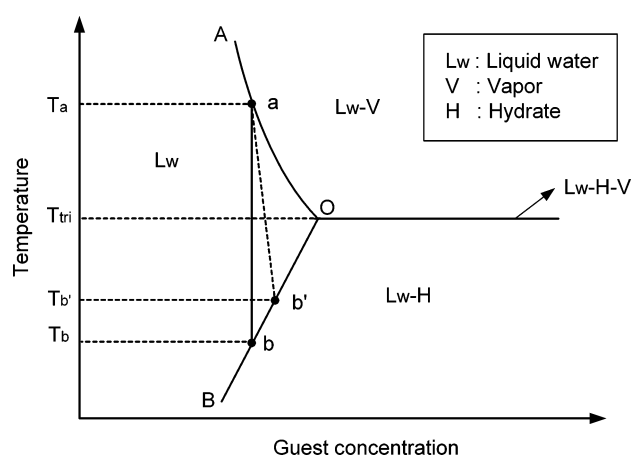


**Figure 15.** Hydrate phase equilibrium (temperature–composition) diagram at constant pressure (adapted from Servio and Englezos<sup>29</sup>).

for hydrate decomposition experiment is to convert fine ice particles into hydrate.<sup>28</sup>

The equilibrium phase diagram in Figure 15, which is adapted from Servio and Englezos,<sup>29</sup> shows regions of stable phases having relatively low guest species composition near three phase temperatures ( $T_{\text{tri}}$ ). Segment OA indicates the solubility of guest molecules in liquid water above  $T_{\text{tri}}$  (liquid water ( $L_w$ )–vapor (V) equilibrium). Similarly, segment OB, which is called liquidus, indicates the solubility of guest molecules in water in



equilibrium with hydrate (H) below  $T_{\text{tri}}$  (Lw–H equilibrium). A typical hydrate formation experiment starts at point *a* in Figure 15, which represents guest species saturated liquid above  $T_{\text{tri}}$ . As the medium temperature is lowered to induce the hydrate formation, the change in the medium state can be represented by a vertical line from point *a* to point *b* if medium composition remained unchanged. As the species transport within the quiescent aqueous solution is much slower compared to the heat transfer, the composition of liquid water away from gas phase changes little during the rapid chilling. No hydrate can form until the medium temperature reaches  $T_b$ , which can be a few degrees lower than  $T_{\text{tri}}$ .<sup>30</sup> Since the liquid contacting the bottom lid is chilled most rapidly due to the high thermal conductivity of SS, the bottom metal wall serves as the preferred location for hydrate crystal nucleation. The homogeneous nucleation within bulk liquid phase is less probable compared to the heterogeneous nucleation at the bottom wall. The slight decrease in system pressure mainly due to the shrinkage of gas phase is neglected in the present discussion for simplicity.

The situation is different for the liquid phase contacting gas phase either at the upper surface of liquid pool or at the surfaces of accidentally included bubbles. The liquid acquires a concentration that is greater than the initial composition during chilling. This process is represented by the dotted line from *a* to *b'* in Figure 15. Since  $T_{b'}$  is higher than  $T_b$ , the formation of hydrate from the liquid contacting gas phase along the upper surface of liquid pool or at the surface of bubble inclusion would occur earlier than hydrate crystallization in bulk liquid if the temperature dropped uniformly. Under the experimental conditions employed in the present study, the hydrate film along the upper surface of the liquid pool always formed prior to the arrival of floating crystals. The migration time required for the floating crystals to reach the hydrate film is estimated longer than 30 min.

Figure 16 shows the schematic profile of temperature and concentration in liquid region in front of growing hydrate as a function of distance from the hydrate/liquid interface. The growth of hydrate crystal differs from the solidification of pure materials, in that the composition of hydrate is not the same as that of the liquid solution from which it is forming. During the solidification of pure materials, there is no net flux of species through the solid/liquid interface as the composition of growing solid is the same as that of adjacent liquid. However, the concentration of guest species in hydrate is much larger than the solubility of the liquid phase in equilibrium. As the hydrate/liquid interface proceeds, the liquid near the interface becomes depleted of guest species. The further growth of the microscopic hydrate/liquid interface must be accompanied by the feed of guest species from the bulk liquid driven by positive concentration gradient near the hydrate/liquid interface (Figure 16a). On the contrary, the latent enthalpy needs to be released at the growing hydrate/liquid interface. As released latent heat needs to be taken over by the surrounding liquid unless it is dissipated through already formed hydrate phase, the temperature gradient is negative near the interface (Figure 16b). Now, local hydrate forming temperature can be calculated from the values of concentration shown in Figure 16a according to the relation between temperature solubility designated as segment OB in Figure 15. The converted hydrate forming temperature is represented by the dashed line in Figure 16b. It is clear that the liquid phase in front of a growing hydrate (hydrate–water interface) is undercooled (constitutional undercooling) because the medium temperature is lower than equilibrium hydrate forming temperature.

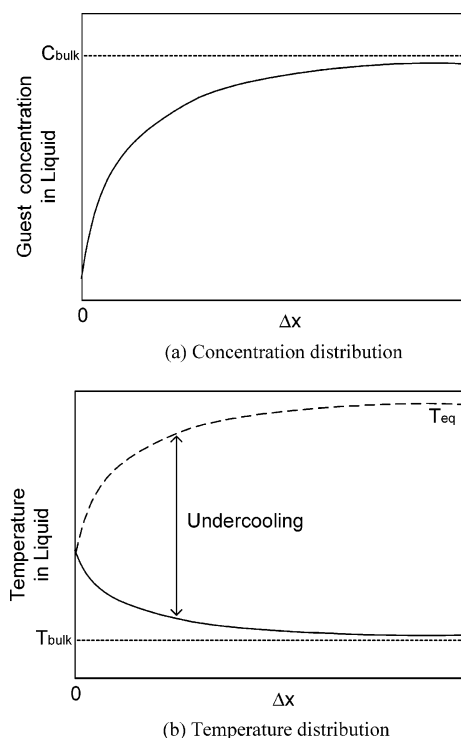


**Figure 16.** Temperature and concentration profiles in the liquid in front of the growing hydrate.  $\Delta x$  is the distance from the hydrate/liquid interface, and  $T_{\text{eq}}$  is the local equilibrium hydrate forming temperature.

If a portion of an originally flat hydrate/liquid interface advances deeper into liquid phase by some disturbances, the liquid in front of the extruded interface becomes more undercooled, resulting in faster local growth rate than neighboring interface. This positive feedback is often called the “Mullins–Sekerka instability”.<sup>31,32</sup> The needlelike extruded crystal had been growing from the hydrate film (Figure 4). The appearance of spicular crystals growing from the hydrate film in Figure 4 is caused by this instability. The growth instability often leads to pattern formations. Among them, the most common mode of crystal growth is the dendritic shape in which treelike microscopic structures develop over an extensive volume (Figures 4–8).

Similarly, the hydrate growth is faster at corners than along neighboring flat interfaces. This concept, originally quoted in metallography as the “corner effect”,<sup>33</sup> explains well the observations contained in Figure 13, in which primary arms always developed from corners of floating crystals. On the contrary, if crystals are growing under a relatively small driving force (undercooling), the corner effect might be insignificant. The rates of crystal growth both on the corner and on the face are comparable. Consequently, floating single crystals retained the octahedral or platelet shapes. The transition from single crystals to more complex dendritic structures is fairly well understood, and theories have been established for various types of solidifications including metals, organic alloys, and snow crystals.<sup>34,35</sup>

## Summary and Conclusions

The dynamics of methane–propane hydrate crystal growth in presaturated liquid water were studied with and without the presence of *n*-heptane under different undercooling conditions. The study revealed various aspects of crystal nucleation, growth, and migration. These results are summarized below.

1. Under all experimental conditions employed in the present study, hydrate film formation at the top surface of liquid water pool was observed first. When undercooling ( $\Delta T$ ) is relatively small ( $\Delta T < 3.2$  K), there is no significant crystal growth from the hydrate film. With intermediate undercooling, a needlelike hydrate grew downward from the hydrate film. As  $\Delta T$  increased, the downward growth of hydrate crystals occurred with a greater rate and with finer spacing. Moreover, when  $\Delta T > 7.2$  K, the growth of hydrate crystals showed a dendritic pattern in which treelike microscopic structures developed from downward growing crystals. As crystal growth progressed, the speed of the downward crystals in the axial direction was decreased, and then thin platelike hydrate crystals developed from the tips and sides of the first-grown hydrate crystals.

2. The small floating crystals were observed regardless of the presence of *n*-heptane and the degree of undercooling. The number of floating crystals is significantly large when memory water is utilized but is not sensitive to the amount of standby time which is smaller than 2 h. The shapes of the floating crystals were diverse and included octahedra and triangular or hexagonal platelets. When the undercooling was small, the octahedral crystals were found dominant. The number of thin triangular platelets was relatively small with even smaller occurrences of hexagonal platelets at the later stage of an experiment run. When  $\Delta T \geq 7.2$  K, the shape of the floating crystals also became dendritic.

3. In the presence of *n*-heptane, the crystal growth characteristics and behavior of floating crystals were qualitatively the same as the methane-propane-water system without *n*-heptane. The downward growth of hydrate below the hydrate film was slower, and the curvature of hydrate film was more noticeable compared to the system without *n*-heptane.

4. The transition from needlelike to dendritic structures of downward growing hydrate crystals and the transition from simple geometric shape into equiaxed dendritic shape of floating crystals are due to the constitutional undercooling (Mullins-Sekerka instability) caused by the interaction between temperature and concentration distribution in front of growing hydrate/liquid interface.

**Acknowledgment.** The financial support from the Natural Sciences and Engineering Research Council of Canada (NSERC) and The Institute of Applied Energy (IAE), Japan, is greatly appreciated. This work was also supported by the research program of Dongguk University. Authors express thanks to Goon-Chul Kim and Joung-Bo Yang from Cheju National University (Korea) for their assistance.

## References

- (1) Davidson, D. W. In *Water: A Comprehensive Treatise*; Frank, F., Ed.; Plenum Press: New York, 1973; Vol. 2, Chapter 3, pp 115–234.
- (2) Sloan, E. D. *Clathrate Hydrates of Natural Gases*, 2nd ed.; Marcel Dekker: New York, 1998.
- (3) Ripmeester, J. A. *Ann. N.Y. Acad. Sci.* **2000**, *912*, 1–16.
- (4) Ripmeester, J. A.; Tse, J., S.; Ratcliffe, C. I.; Powell, B. M. *Nature* **1987**, *325*, 135–136.
- (5) Ripmeester, J. A.; Ratcliffe, C. I. *J. Phys. Chem.* **1990**, *94*, 8773–8776.
- (6) Englezos, P. *Ind. Eng. Chem. Res.* **1993**, *32*, 1251–1274.
- (7) Koh, C. A. *Chem. Soc. Rev.* **2002**, *31*, 157–167.
- (8) Sloan, E. D. *J. Chem. Thermodyn.* **2003**, *35*, 41–53.
- (9) Kaviany, M. *Principles of Heat Transfer in Porous Media*, 2nd ed.; Springer-Verlag: New York, 1999.
- (10) Ohmura, R.; Shimada, W.; Uchida, T.; Mori, Y. H.; Takeya, S.; Nagao, J.; Minagawa, H.; Ebinuma, T.; Narita, H. *Philos. Mag.* **2004**, *84*, 1–16.
- (11) Lee, J. D.; Susilo, R.; Englezos, P. *Chem. Eng. Sci.* **2005**, *60*, 4203–4212.
- (12) Makogon, T. Y.; Larsen, R.; Knight, C. A.; Sloan, E. D. *J. Cryst. Growth* **1997**, *179*, 258–262.
- (13) Larsen, R.; Knight, C. A.; Rider, K. T.; Sloan, E. D. *J. Cryst. Growth* **1999**, *204*, 376–381.
- (14) Smelik, E. A.; King, H. E., *Am. Mineral.* **1997**, *82*, 88–98.
- (15) Servio, P.; Englezos, P. *Cryst. Growth Des.* **2003**, *3*, 61–66.
- (16) Ohmura, R.; Matsuda, S.; Itoh, S.; Ebinuma, T.; Narita, H. *Cryst. Growth Des.* **2005**, *5*, 1821–1824.
- (17) Subramanian, S.; Ballard, A. L.; Kini, R. A.; Dec, S. F.; Sloan, E. D. *Chem. Eng. Sci.* **2000**, *55*, 1981–1999.
- (18) Subramanian, S.; Ballard, A. L.; Kini, R. A.; Dec, S. F.; Sloan, E. D. *Chem. Eng. Sci.* **2000**, *55*, 5763–5771.
- (19) Ballard, A. L.; Sloan, E. D. *Chem. Eng. Sci.* **2000**, *55*, 5773–5782.
- (20) Takeya, S.; Kamata, Y.; Uchida, T.; Nagao, J.; Ebinuma, T.; Narita, H.; Hori, A.; Hondoh, T. *Can. J. Phys.* **2003**, *81*, 479–484.
- (21) Uchida, T.; Moriaki, M.; Takeya, S.; Ikeda, I. Y.; Ohmura, R.; Nagao, J.; Minagawa, H.; Ebinuma, T.; Narita, H.; Gohara, K.; Mae, S. *AIChE J.* **2004**, *50*, 518–523.
- (22) Thomas, S.; Dawe, R. A. *Energy* **2003**, *28*, 1461–1477.
- (23) Ohmura, R.; Kashiwazaki, S.; Shiota, S.; Tsuji, H.; Mori, Y. H. *Energy Fuels* **2002**, *16*, 1141–1147.
- (24) Ohmura, R.; Matsuda, S.; Uchida, T.; Ebinuma, T.; Narita, H. *Cryst. Growth Des.* **2005**, *5*, 953–957.
- (25) Englezos, P.; Kalogerakis, N. E.; Dholabhai, P. D.; Bishnoi, P. R. *Chem. Eng. Sci.* **1987**, *42*, 2647–2658.
- (26) Englezos, P.; Kalogerakis, N. E.; Dholabhai, P. D.; Bishnoi, P. R. *Chem. Eng. Sci.* **1987**, *42*, 2659–2666.
- (27) Clarke, M. A.; Bishnoi, P. R. *Chem. Eng. Sci.* **2005**, *60*, 695–709.
- (28) Genov, G.; Kuhs, W. F.; Staykova, D. K.; Goreschnik, E.; Salamatina, A. N. *Am. Mineral.* **2004**, *89*, 1228–1239.
- (29) Servio, P.; Englezos, P. *J. Chem. Eng. Data* **2002**, *47*, 87–90.
- (30) Buffett, B. A.; Zatssepina, O. Y. *Mar. Geol.* **2000**, *164*, 69–77.
- (31) Mullins, W. W.; Sekerka, R. F. *J. Appl. Phys.* **1964**, *35*, 444–451.
- (32) Langer, J. S. *Rev. Mod. Phys.* **1980**, *51*, 1–28.
- (33) Fleming, M. C. *Solidification Processing*; McGraw-Hill: New York, 1974.
- (34) Murowchick, J. B.; Barnes, H. L. *Am. Mineral.* **1987**, *72*, 1241–1250.
- (35) Libbrecht, K. G. *Rep. Prog. Phys.* **2005**, *68*, 855–895.